Revision_1

Thermal and compressional behavior of the natural borate kurnakovite, $MgB_3O_3(OH)_5 \cdot 5H_2O$

Francesco Pagliaro[a], Paolo Lotti[a*], Tommaso Battiston[a], Davide Comboni[a,b], G. Diego Gatta[a], Fernando Cámara[a], Sula Milani[a], Marco Merlini[a], Konstantin Glazyrin[c], Hanns-Peter Liermann[c]

[a]Dipartimento di Scienze della Terra, Università degli Studi di Milano, Via Botticelli 23, 20133 Milano, Italy

[b]European Synchrotron Radiation Facility, 71 Avenue des Martyrs, CS40220, 38043 Grenoble Cedex, France

[c]Photon Sciences, DESY, PETRA-III, Notkestrasse 85, 22607, Hamburg, Germany

* Corresponding Author: paolo.lotti@unimi.it; Tel: +39-02-50315601; Fax: +39-02-50315598

Abstract

The thermal and compressional behaviors of kurnakovite, a potential B-rich aggregate in neutron radiation-shielding concretes, were studied by *in situ* single-crystal synchrotron X-ray diffraction (100-393 K, 0-13.36(5) GPa). Above 393 K, the crystal structure collapses in response to dehydration. The bulk thermal expansion coefficient is $\alpha_{V(298K)}=5.18(1)\cdot10^{-5}$ K^{-1}. Volume compressional trend modelled with a Birch-Murnaghan equation of state yields a bulk modulus of $K_{P0,T0}=35(3)$ GPa. A phase transition occurs between 9.23(5) and 11.11(5) GPa, leading to a triclinic high-*P* polymorph (with triple unit-cell volume) and to an increase in coordination of one third of the trigonal-planar boron sites to a tetrahedral geometry.

Keywords: Kurnakovite, borates, single-crystal diffraction, B-rich aggregate, high temperature, high pressure

1. Introduction

Natural borates represent the main source for boron, an element used in a variety of different industrial sectors, including glass, ceramics, electronics, metallurgy, textile, cosmetics and chemistry [1]. Boron, mainly in the form of borates and carbides, also finds applications as a fundamental constituent of neutron radiation-shielding materials, which are used in nuclear energy plants, as well as in facilities for scientific research or medical applications, *e.g.* [2-3]. The high capability of borates to act as neutron-shielding materials is due to the isotope ^{10}B, which represents about 20 % of natural boron [4] and has a high cross section for thermal neutrons (~3840 barns [5]), leading to the following reaction:

$$^{10}B + n \rightarrow \alpha + {}^{7}Li + \gamma\,.$$

According to the reaction above, compounds containing boron represent ideal materials to be added as aggregates in the production of radiation-shielding concretes. Synthetic B_4C, for example, proved to be efficiently adopted in this field [6] but, due to the high costs of synthesis, the use of the cheaper natural borates is preferred [7]. Moreover, hydrous borates, due to the capability of hydrogen to act as a neutron acceptor, improve the neutron-shielding efficiency of the material. Recently, a study on neutron permeability of natural borates has been conducted on inyoite, inderite, borax, kurnakovite and colemanite [8]. Kurnakovite has been identified as the most effective natural borate in neutron absorption [8]. Kurnakovite is a complex hydrous magnesium borate mineral, with an ideal chemical formula of $MgB_3O_3(OH)_5 \cdot 5H_2O$, with $B_2O_3 \approx 37$ wt% and $H_2O \approx 48$ wt%. Unlike the Na-bearing

minerals borax [$Na_2B_4O_5(OH)_4 \cdot 8H_2O$] and ulexite [$NaCaB_5O_6(OH)_6 \cdot 5H_2O$], which have already been investigated for the application as B-rich aggregates in concretes (*e.g.* Glinicki et al. [2]), the Na-free kurnakovite cannot release this element, which is well known to promote deleterious reactions (i.e. Alcali-Silica Reactions, ASR) decreasing the durability and the mechanical strength of Portland cements.

Evaporitic sediments and rocks, emplaced in continental lacustrine settings in arid and semiarid environments, are the most common hosts for high-grade boron deposits. Whereas borax, colemanite, ulexite and kernite represent the most diffuse borates of economic importance [9], kurnakovite may also constitute a relevant fraction of the mineralization. For example, kurnakovite is well distributed in the Turkish deposit of Sarıkaya [10-11] and in the Qinghai-Tibet Plateau deposits, where a Mg-enrichment has been reported [12]. Kurnakovite forms for chemical precipitation processes in salt-lake deposits, within brines enriched in magnesium and boron, or for secondary alteration of other Mg-bearing hydrous borates [12-14].

In this light, this study aims at investigating the behavior of natural kurnakovite at varying temperature (*i.e.*, above and below the ambient *T*) and at high pressure, by means of *in situ* single-crystal synchrotron X-ray diffraction. The results will provide thermo-elastic parameters (bulk thermal expansion and compressibility coefficients), to be included in the thermodynamic databases, as well as a description of the thermo-elastic anisotropy, along with the mechanisms, at the atomic scale, that govern that. The phase stability fields of kurnakovite as a function of *T* and *P* will also be reported. In terms of potential applications of this mineral as aggregate in radiation-shielding concretes, due to its hydrous nature, the thermal stability is of a significant relevance, as a *T*-induced dehydration is expected to undermine the durability of the final products. This work is part of a long-term project devoted to characterize the crystal chemistry and explore the *T*- and *P*-behaviors and stability of synthetic B-compounds [15] and natural hydrous borates [16- 21].

1.1 Crystal structure of kurnakovite

Kurnakovite is a member of the inderite group, commonly found in saline lake sediments along with borax and ulexite [22], which was first discovered at the Inder deposit (Kazakhstan). The chemical composition of kurnakovite has been first reported by Godlevsky [23] and, along with inderite, it is one of the two polymorphs of the compound $MgB_3O_3(OH)_5 \cdot 5H_2O$ [24]. Differences between the crystal structures of kurnakovite and inderite have been described by Corazza [25] and recently reported, on the basis of ^{11}B and ^{25}Mg NMR, by Zhou et al. [26]: both inderite and kurnakovite have a crystal structure composed by $Mg(H_2O)_4B_3O_3(OH)_5$ electroneutral units and "zeolitic" H_2O molecules. Inderite has a monoclinic unit-cell (space group $P2_1/c$) and the $Mg(H_2O)_4B_3O_3(OH)_5$-units are organized in independent groups, whereas kurnakovite has a triclinic unit-cell (space group $P\bar{1}$) and its structure is characterized by the presence of chains. The first structural information about kurnakovite were given by Petch et al. [27] and later the crystal structure was solved by Razmanova et al. [28] and refined by Corazza [29], by means of single-crystal X-ray diffraction data collected with a Weissenberg camera. Recently, Gatta et al. [19], using single-crystal neutron diffraction data, provided a full anisotropic structural refinement, including even all the H atoms, and a comprehensive chemical analysis, by means of a multi-methodological approach, which surveyed the presence of 50 chemical elements, yielding a composition of the studied compound very close to the kurnakovite nominal formula. According to the model refined by Corazza [29] and later confirmed by Gatta et al. [19], the neutral $Mg(H_2O)_4B_3O_3(OH)_5$-units are organized in chains running along the [001] direction (Fig. 1). Every chain is made by the alternation of $Mg(OH)_2(H_2O)_4$ octahedra and 3-membered rings of B-polyhedra, which are characterized by one $[BO_2(OH)]$-group in trigonal-planar coordination and two $[BO_2(OH)_2]$-tetrahedra (Fig. 1). Kurnakovite exhibits hydroxyl groups, cation-coordinated H_2O and even loosely-bonded "zeolitic" H_2O molecules, which are hydrogen-bonded to the $Mg(H_2O)_4B_3O_3(OH)_5$-units and populate the cavities confined by the chain system (Figs. 1 and 2).

2. Materials and experimental methods

The crystals used in this study are from the same natural sample of kurnakovite previously studied by Gatta et al. [19]. This sample was provided by the Museum of Mineralogy of the University of Padova (Italy) and comes from the Kramer Deposit, Mohave Desert (Kern County, California, USA). A comprehensive description of the geological setting in which the samples were collected is reported by Noble [30], Siefke [31], Obert & Long [32]. The chemical composition of the investigated samples of kurnakovite, determined on the basis of a multi-methodological approach, is $Mg_{0.99}(Si_{0.01}B_{3.00})_{\Sigma 3.01}O_{3.00}(OH)_5 \cdot 4.98H_2O$, showing an almost perfect agreement with the nominal chemical formula of this mineral. Further details on the experimental protocol for the chemical analysis are reported by Gatta et al. [19].

2.1 Low-temperature and high-temperature X-ray diffraction experiments

In situ low-temperature (*i.e.* $T < 298$ K) and high-temperature ($T > 298$ K) synchrotron single-crystal X-ray diffraction experiments were performed at the XRD1 beamline of the Elettra facility (Trieste, Italy). A single crystal of kurnakovite (80x60x50 μm^3) was loaded in a quartz capillary (100 μm in diameter). A monochromatic and polarized incident X-ray beam, with energy of 17.71 keV ($\lambda = 0.700$ Å), was used. Low-temperature conditions were obtained by means of an Oxford Cryostream 700 cryostat, which provided a continuum cold nitrogen flux on the quartz capillary holding the sample. A first ramp from 100 K to ambient temperature (298 K), with data collections every 20 K, was performed. A second ramp, at high-temperature conditions, was performed by heating the sample *via* a hot gas blower (DGB-0002). The high-temperature ramp ranges from 353 K to 423 K, with data collections every 20 K. Temperature was measured by a thermocouple, previously calibrated using the thermal expansion of quartz. The X-ray diffraction patterns were collected by a Dectris Pilatus 2M detector. The detector-sample distance was 100.05 mm for the low-temperature ramp and 395.28 mm for the high-temperature one. The two sample-detector distances have been calculated using a standard NIST 640e Si powder as calibrant. Data collections at low- and high-temperature were performed adopting the same strategy: each data collection is composed by a step-wise 360° rotation along φ (χ=90°), according to the 4-circle Eulerian geometry, with a step-width of 1° and an exposure time of 1 s/frame.

For both low- and high-T experiments, indexing of the diffraction peaks, unit-cell parameters refinement and intensity data reduction were performed using the CrysAlisPro software [33].

2.2 High-pressure X-ray diffraction experiments

In situ high-pressure (at ambient temperature, 297 K) single-crystal synchrotron X-ray diffraction experiments were performed at the Extreme Conditions Beamline P02.2 at DESY/PETRA-III (Hamburg, Germany). A monochromatic incident X-ray beam with an energy of 42.8 keV (λ=0.2898 Å) was used. A diamond anvil cell (DAC), equipped with Boehler-Almax designed diamonds/seats with 60° opening and 300 μm culets size, was used to generate quasi-hydrostatic pressure. A 250 μm-thick rhenium foil gasket was pre-indented to 60 μm and then drilled by spark erosion, to obtain a cylindrical pressure chamber, 150 μm in diameter. A single crystal of kurnakovite (20x20x15 μm^3), along with a few ruby micro-spheres as pressure calibrants (pressure uncertainty ± 0.05 GPa [34, 35]), were loaded in the pressure chamber. For each P-point, the same data collection strategy was used, consisting in a step-wise ω-scan ($-30° < \omega < +30°$) with a step-width of 0.5° and an exposure time of 1 s/frame. At ambient conditions, the X-ray diffraction pattern was collected with the crystal loaded in the DAC without any P-transmitting fluid. Then, neon was used as quasi-hydrostatic pressure-transmitting fluid [36] and the pressure increase was controlled by an automated pressure-driven system. X-ray diffraction patterns were collected on a PerkinElmer 1621 XRD flat-panel detector, set at a distance of 395.38 mm from the sample. The sample-to-detector distance was calibrated using a CeO_2 standard (NIST 674a). Experimental data were collected using an in-house script and then

converted to the "Esperanto" format in order to be processed by the CrysAlisPro software [33, 37], for the indexing of the X-ray diffraction peaks, unit-cell refinements and intensity data reduction (corrected for Lorentz-polarization effects). Absorption effects, due to the DAC components, were corrected using the semi-empirical *ABSPACK* routine, implemented in CrysAlisPro.

2.3. Structure refinements

The experimental X-ray diffraction patterns collected at ambient conditions were compatible with the space group $P\bar{1}$ and the unit-cell parameters of kurnakovite reported by Corazza [29].

All structure refinements were performed using the software Jana2006 [38], starting from the model reported by Gatta et al. [19] in the space group $P\bar{1}$. On the basis of the reported chemical purity of the investigated sample [19], all the crystallographic sites were modelled as fully occupied, using the Mg, B and O neutral scattering curves [39]. For the high-pressure data, in order to reduce the number of refined variables, the atomic displacement parameters (ADP) were all refined as isotropic. Due to the reciprocal lattice coverage limitations induced by the limited opening angle in the DAC, an H-free structure model was used for all the high-*P* refinements. The atomic fractional coordinates and ADP parameters refined from three selected datasets of kurnakovite (P_{amb}, 4.43(5) and 8.08(5) GPa) and one (at 11.11(5) GPa) of kurnakovite-II, the H*P* polymorph (see section 3.3 for further details), are reported in Tab. 1 and Tab. 2, respectively. The structure refinements based on the H*T* and L*T* data were performed adopting anisotropic displacement parameters, except for the H-atoms (for which displacement parameters were kept constant, with U_{iso} = 0.037 Å^2), and refining the extinction factor by means of an anisotropic model. The refined atomic fractional coordinates and ADPs at three different temperature conditions (100, 297 and 393 K) are reported in Tab. 3 and Tab. S1 (supplementary materials), respectively. All the refinements converged with no significant correlations among the refined variables. A selection of relevant statistical parameters pertaining to the structure refinements at H*P*, H*T* and L*T* is reported in Tab. 4. The results of all the structure refinements are deposited as Supplementary materials (CIF files).

3. Results and discussion

3.1 Thermal behavior and dehydration

The evolution of the unit-cell parameters of kurnakovite with *T* shows that no phase transition occurs in the *T*-range investigated, up to the complete amorphization of kurnakovite observed at a temperature higher than 393 K (Tab. 5, Fig. 3). At this temperature, the diffraction pattern can still be indexed, but more than 90% of the X-ray diffraction peaks are lost; at 423 K no discrete reflections in the X-ray diffraction pattern are observed. The (X-ray)-amorphization temperature of kurnakovite shows a good agreement with a previous H*T*-study conducted by means of thermogravimetric (TG) analysis coupled with DTA, which reports a strong dehydration peak at ca. 412 K [8]. The weight loss measured by Derun & Kipcak [8], 44.58 %, is very close to the total fraction of H_2O determined by Gatta et al. [19] for the same sample of kurnakovite investigated in this study (48.2(2) wt%). Tab. 5 and Fig. 3 report the evolution of the unit-cell parameters with temperature, showing an anisotropic thermo-elastic behavior. The unit-cell edge parallel to [010] shows the minor variation, especially below the ambient temperature. The bulk thermal expansion is substantially accommodated along the *a* and *c* unit-cell axes, which both show a similar thermal expansivity in the investigated *T*-range (Fig. 3).

In order to model the bulk thermal expansion of kurnakovite, a modified version of the equation of state of Pawley et al. [40], reported by Holland & Powell [41], was fitted to the experimental *V*-*T* data, using the *Eos_Fit7c* software [42, 43]. The adopted equation of state is expressed as:

$$V_T = V_0\left(1 + \alpha_0\left(T - T_{ref}\right) - 2(10\alpha_0 + \alpha_1)\left(\sqrt{T} - \sqrt{T_{ref}}\right)\right),$$

where T_{ref} = 298 K, V_0 is the unit-cell volume at T_{ref} and α_0 and α_1 are refinable parameters.

The fit to the experimental data yields the following refined parameters: α_0 = 12.9(3)·10^{-5} K^{-1}, α_1 = -2.2(2)·10^{-4} K$^{-1/2}$ and V_0 = 500.51(2) Å^3. The calculated bulk thermal expansion coefficient at ambient conditions is $\alpha_{V(298K)}$ = 5.18(1)·10^{-5} K^{-1}. The mean thermal expansivity values along the axes of the unit-strain ellipsoid have been determined between 100 and 393 K, using the *Win_Strain* software [44], showing a dramatic thermal anisotropy: α_1 = 3.7(1)·10^{-5} K^{-1}, α_2 = 1.8(1)·10^{-5} K^{-1} and α_3 = 0.10(5)·10^{-5} K^{-1}. The geometrical relationships between the unit-strain ellipsoid and the crystallographic axes are described by the following matrix:

$$\begin{pmatrix}\alpha_1\\ \alpha_2\\ \alpha_3\end{pmatrix} = \begin{pmatrix}59.2(5)^\circ & 71.2(4)^\circ & 68.4(8)^\circ\\ 40.9(9)^\circ & 93.4(7)^\circ & 150(1)^\circ\\ 65.8(6)^\circ & 160.9(3)^\circ & 70.0(8)^\circ\end{pmatrix}\cdot\begin{pmatrix}a\\ b\\ c\end{pmatrix}$$

which agrees with the low thermal expansivity shown by the *b* unit-cell parameter (Fig. 3 and Tab. 5), given the 19.1(3)° angle between α_3 and $[0\bar{1}0]$.

The structure refinements based on the XRD data collected at different *T* conditions do not show any significant structural re-arrangement between 100 and 393 K, nor a change in the H-bonding configuration. Analysis of the *T*-induced evolution of the interatomic distances between the oxygen *donors* (D) and *acceptors* (A) (Tab. S2) shows that, with few exceptions, the D-A distances expand with increasing temperature. This behavior suggests that the collapse of the H-bonding network plays a key role in triggering the amorphization of kurnakovite at $T > 393$ K, similarly to the behavior shown in colemanite, for which the amorphization occurs in the very early stages of dehydration at $T > 513$ K [18].

3.2 High-pressure behavior

The high-pressure evolution of the unit-cell parameters is shown in Tab. 6 and Fig. 4. The ambient-conditions polymorph of kurnakovite is found to be stable up to 9.23(5) GPa. Above this pressure, a phase transition to a high-pressure polymorph, which will be discussed in the next section, occurs. A Birch-Murnaghan Equation of State truncated to the third order (BM3-EoS) [45, 46] was fitted to the experimental *P*-*V* data of the ambient-conditions polymorph, using the *Eos_Fit7c* software [43]. The BM-EoS is an isothermal equation of state based on the assumption that the high-pressure strain energy of a solid can be expressed as a Taylor series in the Eulerian finite strain, defined as $fe = [(V_0/V)^{2/3} - 1]/2$. This equation of state allows to refine the bulk modulus ($K_{P0,T0} = -V_0(\partial P/\partial V)_{T0} = \beta^{-1}_{P0,T0}$, where $\beta_{P0,T0}$ is the volume compressibility coefficient at ambient conditions) and its *P*-derivatives. When truncated to the third order, the BM3-EoS is expressed as:

$$P(fe) = 3K_{P0,T0}\, fe\, (1 + 2fe)^{5/2}\, [1 + 3/2(K' - 4)fe\,],$$

where $K' = \partial K_{P0,T0}/\partial P$.

The fit of the BM3-EoS to the experimental data yields the following refined parameters: $K_{P0,T0}$ = 35(3) GPa, K' = 6.3(1) and V_0 = 498.8(2) Å^3

Fig. 4 shows that the elastic deformation of kurnakovite at high pressure is significantly anisotropic, with [010] being the most compressible crystallographic direction. The analysis of the finite Eulerian unit-strain tensor, performed using the software *Win_Strain* [44], allowed to calculate the mean compressibility values along the axes of the strain ellipsoid determined between 0.0001 and 9.23 GPa: ε_1 = 0.00920(6) GPa^{-1}, ε_2 = 0.00515(6) GPa^{-1}, ε_3 = 0.00299(12) GPa^{-1}. The geometrical relationships between the strain ellipsoid and the crystallographic axes are described by the following matrix:

222 $$\begin{pmatrix}\varepsilon_1\\ \varepsilon_2\\ \varepsilon_3\end{pmatrix} = \begin{pmatrix}114.9(5)^\circ & 14.8(7)^\circ & 86.3(7)^\circ\\ 72(2)^\circ & 76.8(5)^\circ & 176.2(6)^\circ\\ 148(1)^\circ & 96.5(6)^\circ & 90(2)^\circ\end{pmatrix}\cdot\begin{pmatrix}a\\ b\\ c\end{pmatrix}$$

223 which shows that the most compressible direction almost coincides with the *b* crystallographic axis,
224 given the low angle between them, *i.e.* 14.8(7)°.

225 Structure refinements of the ambient-conditions polymorph of kurnakovite, based on the XRD data
226 collected between room-*P* and 9.23(5) GPa, allowed to describe the structural mechanisms acting at
227 the atomic scale which controls the bulk compression. Tab. S3 shows that the B coordination
228 environments are substantially uncompressible, whereas the shortening of Mg-φ bond distances (φ =
229 O, OH, OH_2) leads to the compression of the Mg coordination polyhedra (Tab. 7). A Birch-Murnaghan
230 equation of state (truncated to the second order) was used to fit the V_{Mg}-*P* data (Tab. 7), using the
231 *EoS_Fit7c* software [40], yielding the following refined bulk modulus for the Mg-polyhedron at
232 ambient conditions: K_{VMg} = 73(4) GPa. The bulk volume compression is, therefore, accommodated by
233 the Mg coordination polyhedra and by the tilting of the other structural units. Only a subtle structural
234 re-arrangement is observed along the direction of the chains made by the Mg- and B-polyhedra, as
235 suggested by the evolution of the B1-Mg1-B1 angle (Figs. 2 and 4; Tab. 8), which shows a slight
236 increase from 147.86(2)° at atmospheric pressure to 149.2(2)° at 9.23(5) GPa. The interchain
237 structural re-arrangement is more pronounced, as suggested by the compression of the O12-O12-O12
238 angle (Figs. 2 and 4; Tab. 8), which reflects the *P*-induced "interpenetration" of adjacent chains,
239 leading to a partial overlap of adjacent borate rings, along a direction almost parallel to the *b*
240 crystallographic axis, in agreement with magnitude and orientation of the unit-strain ellipsoid.
241 Interestingly, a "non-inverse" behavior (*sensu* Hazen and Finger [47]) is not shown at varying
242 temperature as seen in section 3.1. On the contrary, the *b* crystallographic axis is the less affected by
243 the thermal variation. The striking difference between the compressional and thermal behavior along
244 the [010] direction is likely ascribable to the pervasive H-bonding network, which allows the
245 compression through the "interpenetration" of adjacent chains, but may prevent the expansion due to
246 an already stretched configuration of the H-bonds (Tab. S2). Unfortunately, due to the modest X-ray
247 scattering power of H-atoms and the limited reciprocal lattice coverage caused by the opening angle
248 of the DAC, hydrogen sites cannot be included in the high-*P* structure refinements, hindering a more
249 detailed discussion on the role played by the H-bonding network (Fig. 2) on the high-pressure
250 structural re-arrangement of kurnakovite.

251 ## 3.3 High-pressure phase transition

252 As mentioned above, between 9.23(5) and 11.11(5) GPa a single-crystal to single-crystal phase
253 transition, reconstructive in character and with an increase of ~3% in density, occurs without any
254 change in the space group, which remains $P\bar{1}$. However, the high-*P* polymorph, hereafter named
255 kurnakovite-II, is characterized by the tripling of the unit-cell volume: the unit-cell parameters of
256 kurnakovite-II at 11.11(5) GPa are the following: *a* = 11.012(2) Å, *b* = 10.827(2) Å, *c* = 11.286(2) Å,
257 α = 99.65(1)°, β = 93.96(2)°, γ = 112.45(2)° and *V* = 1212.8(3) $Å^3$. The geometrical relationships
258 between the unit cells of kurnakovite and kurnakovite-II are described by the following matrix:

259 $$\begin{pmatrix}a'\\ b'\\ c'\end{pmatrix} = \begin{pmatrix}-1 & -1 & 0\\ 0 & 1 & 1\\ -1 & 0 & -2\end{pmatrix}\begin{pmatrix}a\\ b\\ c\end{pmatrix}$$

260 where *a'*, *b'* and *c'* refer to kurnakovite-II, whereas *a*, *b* and *c* refer to kurnakovite. The unit-cell
261 parameters of kurnakovite-II refined at 11.11(5), 12.21(5) and 13.63(5) GPa are reported in Tab. 6.
262 Furthermore, the unit-cell parameters of kurnakovite-II can also be described in a different setting
263 (according to the ambient-conditions polymorph geometry) given in Tab. S4.

The kurnakovite-II crystal structure has been successfully solved using the SUPERFLIP suite [48] implemented in JANA2006, which allowed to locate most of the crystallographic sites. Then, after a series of least-squares refinements followed by difference-Fourier syntheses of the electron density, the location of the missing atoms was achieved. The tripling of the unit-cell volume implies the split of any independent atomic-sites of kurnakovite into three independent sites in kurnakovite-II: 3 independent magnesium, 9 boron and 39 oxygen sites.

From the structural point of view, the phase transition does not induce dramatic changes. The crystal structure can still be described by infinite chains of alternating Mg-polyhedra and 3-membered rings of B-polyhedra. Unfortunately, the inability to locate the H atoms prevents a robust discussion on the inter-chains connection via the H-bonding network. The tripling of independent sites of kurnakovite implies that, in the H*P*-polymorph, the chains are characterized by the repetition of units made by three independent Mg-polyhedra and three independent borate rings, providing more degrees of freedom for a moderate intra-chain distortion with respect to kurnakovite (Fig. 5). The most significant consequence of the phase transition concerns one of the three B sites derived from the parent trigonal-planar B3. The B33 atom increases its coordination configuration from trigonal-planar to tetrahedral, by bonding with the O43 atom that belongs already to a H_2O molecule in the coordination sphere of the Mg13 atom (Fig. 5). The formation of this new bond requires only a local distortion of the crystal structure, resulting in the preservation of the long-range order, as confirmed by the single-crystal to single-crystal nature of the phase transition. A similar behavior was also shown by colemanite [$CaB_3O_4(OH)_3 \cdot H_2O$], which underwent a $P2_1/a$-to-$P2_1/a$ phase transition between 13.95 and 14.91 GPa, with a unit-cell volume of the high-*P* polymorph that is 6 times the low-*P* one, and in which any parent crystallographic site generates six new independent sites [16]. Also in colemanite, a fraction of trigonal-planar B increases its coordination to tetrahedral by bonding to a H_2O-oxygen atom in colemanite-II; an increase in the coordination number of a fraction of the Ca sites was also observed. Similarly, kernite [$Na_2B_4O_6(OH)_2 \cdot 3H_2O$], undergoes a $P2_1/c$-to-$P2_1/c$ phase transition, isosymmetric in character, between 1.6 and 2.0 GPa [21], which involves an increase in the coordination number of the Na atoms, whereas no change in the coordination environments of B was observed. A second phase transition, apparently isosymmetric, was observed between 6.6 and 7.5 GPa, but any attempt to solve the crystal structure of kernite-III was unsuccessful [21].

When compared to the aforementioned borates, the phase transition shown by kurnakovite in this study is more closely related to that observed in colemanite, because of the very high pressures it occurs and due to the increase in the coordination number of a fraction of B sites from three to four. On the contrary, in the Na-bearing kernite, a *P*-induced phase transition occurs at lower pressure, involving only the coordination environment of the monovalent cation. These results shed a new light on the high-pressure behavior of B-bearing hydrous compounds, highlighting the potential role that monovalent or divalent cations can play.

Any discussion on the high-*P* structure evolution of kurnakovite-II is hindered by the fact that, at the highest investigated pressure (13.63(5) GPa), a drastic reduction of "observed" peaks (*i.e.* with $I_{hkl} \geq 3\sigma(I_{hkl})$) prevented any attempt of structure refinement. Data collected in decompression at 10.80(5) and 8.29(5) GPa allowed the indexing of the few diffraction peaks and the refinement of the unit-cell parameters (Tab. 6), which suggest a significant hysteresis of the transition; no structure refinement was performable. Interestingly, the data collected after decompression at ambient-*P* (after full release of *P*) showed the absence of any diffraction pattern, indicating the irreversible nature of the phase transition and a structural collapse of kurnakovite-II upon full pressure release.

4. Conclusions

The present study allowed the characterization, for the first time, of the thermo-elastic behavior of kurnakovite, which could serve as a potential aggregate in neutron radiation-absorber concretes. Kurnakovite shows a significant thermal anisotropy with the bulk expansion being mainly accommodated along the *a* and *c* crystallographic directions. Under pressure, kurnakovite shows a similar anisotropic elastic behavior, but the direction of higher compressibility almost coincides with the *b* crystallographic axis. The bulk thermal expansion coefficient and the bulk compressibility of kurnakovite at ambient conditions are provided along with their evolution as a function of temperature and pressure, respectively. Based on these data, we can provide a *P*-*V*-*T* equation of state, valid at a first approximation:

$$V(P,T) = V_0 + 5.18(1)\cdot 10^{-5}*(T - T_0) - 0.029(2)*(P - P_0);$$

where T_0 and P_0 are 298 K and 0.0001 GPa, respectively, and V_0 the unit-cell volume at ambient conditions.

The XRD data obtained at high-*T* in this study, in agreement with the previous TG and DTA data reported by Derun & Kipcak [8], show that, due to the dehydration phenomena, the crystal structure of kurnakovite is unstable at $T > 393$ K and is completely amorphized at 423 K. This behavior poses severe questions on the potential applicability of kurnakovite, as is, in radiation-shielding concretes. Despite several operating conditions do not reach temperatures higher than ~373 K [*i.e.* ~100 °C; see *e.g.* Lotti et al. [18] and references therein], the observed structural degradation at 393 K would suggest to consider alternative neutron absorber minerals for any application which should sustain non-ambient temperature conditions. In this context, one may consider the highest thermal stability of natural colemanite (at least up to 513 K [18]) as a suitable alternative. However, a transformation product (*e.g.* a dehydrated form) of kurnakovite could still be considered.

At high pressure, kurnakovite is stable under the conditions for any technical utilization. The *P*-induced structural re-arrangement of kurnakovite sheds a new light on the intriguing high-pressure behavior of hydrous natural borates. Kurnakovite undergoes a reconstructive phase transition between 9.23(5) and 11.11(5) GPa towards a polymorph, kurnakovite-II, still triclinic but with a unit-cell volume three times larger with respect to kurnakovite. As in colemanite [16], the high-*P* phase transition induces a fraction of the trigonal-planar B atoms to increase their coordination to tetrahedral, with a new bond with a H_2O-oxygen. However, unlike Ca in colemanite and Na in kernite [21], no re-arrangement of the Mg-coordination has been observed in kurnakovite in response to the *P*-induced phase transition.

The structural evolution of borates at high pressure may open a new window to understand the *P*-induced trigonal-planar-to-tetrahedral transition of C coordination reported to occur at much higher pressures (*e.g.* [49]), which is of large relevance in Earth science and in materials science.

5. Acknowledgments

Three anonymous reviewers are gratefully thanked for the fruitful and competent suggestions, which helped to increase the manuscript quality. Alessandro Guastoni (University of Padova) is thanked for the provision of the kurnakovite sample. Maurizio Polentarutti and Giorgio Bais are thanked for the support at the XRD1 beamline. Elettra Sincrotrone Trieste and DESY-Petra-III at Hamburg are acknowledged for the allocation of beamtime. Parts of this research were carried out at P02.2 at DESY, a member of the Helmholtz Association (HGF). The research leading to this result has been supported by the project CALIPSOplus under the Grant Agreement 730872 from the EU Framework Programme for Research and Innovation HORIZON 2020. FP, PL, TB, DC, FCA, GDG, SM and MM acknowledge the support from the Italian Ministry of Education (MIUR) through the projects: "*Dipartimenti di Eccellenza 2018-2022*", "PRIN2017 - Mineral reactivity, a key to understand large-

scale processes" (2017L83S77), and University of Milano "La Statale" through the project "*Piano di sostegno alla ricerca 2018*".

6. References

[1] D. Bernhardt, I.I. Reilly, Mineral Commodity Summaries 2019, US Geological Survey, Reston, USA, 2019.

[2] M.A. Glinicki, A. Antolik, M. Gawlicki, Evaluation of compatibility of neutron-shielding boron aggregates with Portland cement in mortar, Constr. Build. Mater. 164 (2018) 731-738.

[3] M.K.A. Roslan, M. Ismail, A.B.H. Kueh, M.R.M Zin, High-density concrete: Exploring Ferro boron effects in neutron and gamma radiation shielding, Constr. Build. Mater. 215 (2019) 718-725.

[4] M.R. Palmer, G.H. Swihart, Boron isotope geochemistry: an overview, in: E.S. Grew and L.M. Anovitz (Eds.), Boron Mineralogy, Petrology and Geochemistry, Rev. Mineral., 33, 1996, pp. 709-744.

[5] R.S. Carter, H. Palevsky, V.W. Myers, D.J. Hughes, Thermal neutron absorption cross sections of boron and gold, Phys. Rev. 92 (1953) 716.

[6] D.D. Di Julio, C.P. Cooper-Jensen, H. Perrey, K. Fissum, E. Rofors, J. Scherzinger, P.M. Bentley, A polyethylene-B_4C based concrete for enhanced neutron shielding at neutron research facilities, Nucl. Instrum. Methods Phys. Res., Sect. A 859 (2017) 41-46.

[7] K. Okuno, M. Kawai, H. Yamada, Development of novel neutron shielding concrete. Nucl. Technol. 168 (2009) 545-552.

[8] E. Derun, A. Kipcak, Characterization of some boron minerals against neutron shielding and 12 year performance of neutron permeability, J. Radioanal. Nucl. Chem. 292 (2012) 871-878.

[9] S.B. Carpenter, R.B. Keistler, Boron and Borates, in: J.E. Kogel, N.C. Trivedi, J.M. Barker, S.T. Krukowski, (Eds.) Industrial minerals & rocks: commodities, markets, and uses, 2006, pp. 275-283.

[10] O. Baysal, New hydrous magnesium-borate minerals in Turkey: kurnakovite, inderite, inderborite, Maden Tetkik ve Arama Dergisi, 80 (1973) 1-12.

[11] I. Koçak, Ş. Koç, Geochemical characteristics of Kırka (Sarıkaya) borate deposit, northwestern Anatolia, Turkey, J. Earth Syst. Sci. 125 (2016) 147-164.

[12] X. Li, S. Gao, Z. Liu, S. Xia, Kurnakovite deposits on the Qinghai-Tibet Plateau (II): an investigation from chemical kinetics of chloropinnoite dissolution, Environ. Earth Sci. 70, (2013) 1151-1158.

[13] Z.H. Liu, S.P. Xia, S.Y. Gao, Studies on the Kinetics of Dissolution and Transformation of [$2MgO{\cdot}2B_2O_3{\cdot}MgCl_2{\cdot}14H_2O$] in water at 60°C, Chem. Res. Chin. Univ. 20 (1999) 186-189.

[14] J. Zuo, Z.H. Liu, Phase Equilibria of the $2MgO{\cdot}2B_2O_3{\cdot}MgCl_2{\cdot}14H_2O$+3.0%$H_3BO_3$+$H_2O$ System at Various Temperatures, J. Chem. Eng. 55, (2010) 5280-5282.

[15] G.D. Gatta, P. Lotti, M. Merlini, H.P. Liermann, M. Fisch, High-Pressure Behavior and Phase Stability of Al_5BO_9, a Mullite-Type Ceramic Material, J. Am. Cer. Soc. 96 (2013) 2583-2592.

[16] P. Lotti, G.D. Gatta, D. Comboni, G. Guastella, M. Merlini, A. Guastoni, H.P. Liermann, High-pressure behavior and P-induced phase transition of $CaB_3O_4(OH)_3{\cdot}H_2O$ (colemanite), J. Am. Cer. Soc. 100 (2017) 2209-2220.

[17] P. Lotti, G.D. Gatta, N. Demitri, G. Guastella, S. Rizzato, M.A. Ortenzi, F. Magrini, D. Comboni, A. Guastoni, M.T. Fernandez-Diaz, Crystal chemistry and temperature behavior of the natural hydrous borate colemanite, a mineral commodity of boron, Phys. Chem. Miner. 45 (2018) 405-422.

[18] P. Lotti, D. Comboni, L. Gigli, L. Carlucci, E. Mossini, E. Macerata, M. Mariani, G.D. Gatta, Thermal stability and high-temperature behavior of the natural borate colemanite: An aggregate in radiation-shielding concretes, Constr. Build. Mater. 203 (2019) 679-686.

[19] G.D. Gatta, A. Guastoni, P. Lotti, G. Guastella, O. Fabelo, M.T. Fernandez-Diaz, A multi-methodological study of kurnakovite: A potential B-rich aggregate, Am. Mineral. 104 (2019) 1315-1322.

[20] G.D. Gatta, A. Guastoni, P. Lotti, G. Guastella, O. Fabelo, M.T. Fernandez-Diaz, A multi-methodological study of kernite, a mineral commodity of boron, Am. Mineral., *in press*, (2020) DOI: http://dx.doi.org/10.2138/am-2020-7433.

[21] D. Comboni, F. Pagliaro, G.D. Gatta, P. Lotti, S. Milani, M. Merlini, T. Battiston, K. Glazyrin, H.P. Liermann, High-pressure behaviour and phase stability of $Na_2B_4O_6(OH)_2 \cdot 3H_2O$ (kernite). J. Am. Cer. Soc. *in press*, (2020) DOI: 10.1111/jace.17185.

[22] C. Helvaci, M.R. Palmer, Origin and distribution of evaporite borates: the primary economic sources of boron. Elements 13 (2017) 249-254.

[23] M.N. Godlevsky, Kurnakovite, a new borate, in: Comptes Rendus (Doklady) de l'Academie des Sciences de l'URSS, Vol. 28, 1940, pp. 638-640.

[24] W.T. Schaller, M.E. Mrose, The naming of the hydrous magnesium borate minerals from Boron, California - a preliminary note, Am. Mineral. 45 (1960) 732-734.

[25] E. Corazza, Inderite: crystal structure refinement and relationship with kurnakovite, Acta Crystallogr. B32 (1976) 1329-1333.

[26] B. Zhou, V.K. Michaelis, Y. Pan, Y. Yao, K.T. Tait, B.C. Hyde, S. Kroeker, Crystal structure refinements of borate dimorphs inderite and kurnakovite using ^{11}B and ^{25}Mg nuclear magnetic resonance and DFT calculations, Am. Mineral. 97 (2012) 1858-1865.

[27] H.E. Petch, K.S. Pennington, J.D. Cuthbert, On Christ's postulated boron-oxygen polyions in some hydrated borates of unknown crystal structures, Am. Mineral. 47 (1962) 401-404.

[28] Z.P. Razmanova, I.M. Rumanova, N.V. Belov, Crystalline structure of kurnakovite $Mg_2B_6O_{11} \cdot 15H_2O = 2Mg[B_3O_3(OH)_5] \cdot 5H_2O$, in: Russian Academy of Sciences, *Doklady Akademii Nauk*, Vol. 189, No. 5, 1969, pp. 1003-1006.

[29] E. Corazza, The crystal structure of kurnakovite: a refinement, Acta Crystallogr. B30 (1974) 2194-2199.

[30] L.F. Noble, Borate Deposits in the Kramer District, Kern County, California, USGS Bulletin 785-C (1926) 45-61.

[31] J.W. Siefke, The Boron open pit mine at the Kramer borate deposit. The Diversity of Mineral and Energy Resources of Southern California, Soc. Econ. Geol. Guidebook Ser. 12 (1991) 4-15.

[32] L. Obert, A.E. Long, Underground Borate Mining, Kern County, Calif, United States Department of the Interior, Bureau of Mines, 1962.

[33] Rigaku Oxford Diffraction, CrysAlisPro Software system, version 1.171.40.67a, Rigaku Corporation, Wroclaw, Poland, 2019.

436 [34] H.K. Mao, J.A. Xu, P.M. Bell, Calibration of the ruby pressure gauge to 800 kbar under quasi-
437 hydrostatic conditions, J. Geophys. Res. 91 (1986) 4673-4676.

438 [35] J.C. Chervin, B. Canny, M. Mancinelli, Ruby-spheres as pressure gauge for optically transparent
439 high pressure cells, High Press. Res. 21 (2001) 305-314.

440 [36] Y. Fei, A. Ricolleau, M. Frank, K. Mibe, G. Shen, V. Prakapenka, Toward an internally consistent
441 pressure scale, Proc. Natl. Acad. Sci. 104 (2007) 9182-9186.

442 [37] A. Rothkirch, G.D. Gatta, M. Meyer, S. Merkel, M. Merlini, H.P. Liermann, Single-crystal
443 diffraction at the Extreme Conditions beamline P02.2: procedure for collecting and analyzing high-
444 pressure single-crystal data, J. Synchrotron Radiat. 20 (2013) 711-720.

445 [38] V. Petříček, M. Dušek, L. Palatinus, Crystallographic computing system JANA2006: general
446 features, Z. Kristallogr. 229 (2014) 345-352.

447 [39] E.N. Maslen, A.G. Fox, M.A. O'Keefe, X-ray scattering, in: E. Prince (Ed.) International Tables
448 for Crystallography Volume C: Mathematical, physical and chemical tables, Kluwer Academics,
449 Dordrecht, 2006, pp. 554-590.

450 [40] A. R. Pawley, S. A. T. Redfern, T. J. B. Holland, Volume behavior of hydrous minerals at high
451 pressure and temperature: I. Thermal expansion of lawsonite, zoisite, clinozoisite, and diaspore, Am.
452 Mineral. 81 (1996) 335-340.

453 [41] T.J.B. Holland, R. Powell, An internally consistent thermodynamic data set for phases of
454 petrological interest, J. Metamorph. Geol. 16 (1998) 309-343.

455 [42] R.J. Angel, J., Gonzalez-Platas, M. Alvaro, EosFit7c and a Fortran module (library) for equation
456 of state calculations, Z. Kristallogr. 229 (2014) 405-419.

457 [43] J. Gonzalez-Platas, M. Alvaro, F. Nestola, R. Angel, EosFit7-GUI: a new graphical user interface
458 for equation of state calculations, analyses and teaching, J. Appl. Crystallogr. 49 (2016) 1377-1382.

459 [44] Angel, R. J. (2011) Win_Strain. A program to calculate strain tensors from unit-cell parameters.
460 http://www.rossangel.com/home.htm

461 [45] F. Birch, Finite elastic strain of cubic crystals, Phys. Rev. 71, (1947) 809-824.

462 [46] R.J. Angel, Equations of state, in: R.M. Hazen, R.T. Downs (Eds.), High-Temperature and High-
463 Pressure Crystal Chemistry, Rev. Mineral. Geochem. 41, 2000, pp. 35-60.

464 [47] R.M. Hazen, L.W. Finger, Comparative crystal chemistry, Am. Sci. 72, (1984) 143-150

465 [48] L. Palatinus, G. Chapuis, SUPERFLIP - a computer program for the solution of crystal structures
466 by charge flipping in arbitrary dimensions, J. Appl. Crystallogr. 41 (2007) 786-790

467 [49] M. Merlini, S. Milani, J. Maurice, Structures and Crystal Chemistry of Carbonate at Earth's
468 Mantle Conditions, in: C.E. Manning, J.F. Lin, W.L. Mao (Eds.), Carbon in Earth's Interior,
469 Geophysical Monograph 249, 2020, pp. 87-95.

470 [50] K. Momma, F. Izumi, VESTA 3 for three-dimensional visualization of crystal, volumetric and
471 morphology data, J. Appl. Crystallogr. 44 (2011) 1272-1276.

472

473

474

475

476

477

478 **Figures captions**

479

480 **Figure 1**: (**a**) the $Mg(H_2O)_4B_3O_3(OH)_5$ unit; (**b**,**c**,**d**) three different views of the crystal structure of
481 kurnakovite (displacement ellipsoid probability factor: 50%).

482

483 **Figure 2**: (**a**) the H-bonding network of kurnakovite; (**b**) a view of the crystal structure of
484 kurnakovite showing the B1-Mg1-B1 and O12-O12-O12 angles.

485

486 **Figure 3**: (**a**) *T*-induced evolution of the unit-cell parameters of kurnakovite, normalized to their
487 ambient-*T* values; (**b**) unit-cell volume *vs*. *T* evolution and the refined Holland-Powell equation of
488 state (see section 3.1 for further details).

489

490 **Figure 4**: (**a**) *P*-induced evolution of the unit-cell volumes of kurnakovite and kurnakovite-II
491 (normalized to kurnakovite, *i.e.* equal to $V_{kur\text{-}II}/3$) and the refined BM3-EoS pertaining to kurnakovite
492 (see section 3.2 for further details); (**b**): *P*-induced evolution of the unit-cell parameters of
493 kurnakovite, normalized to their ambient-*P* values; (**c**) Variation with pressure of the B1-Mg1-B1 and
494 O12-O12-O12 angles, normalized to their values at ambient-*P*; (**d**) Evolution of the Mg1-O1, Mg1-
495 O5 and Mg1-O6 bond distances (normalized to their ambient-*P* values) with pressure.

496

497 **Figure 5**: Comparison between the chain configuration in kurnakovite (**a**) and kurnakovite-II (**b**). The
498 phase transition induces one third of the B3 atomic sites in trigonal-planar coordination (shown in
499 purple) to gain a tetrahedral coordination in kurnakovite-II (*i.e.,* B33 shown in purple), by making a
500 new bond with a H_2O-oxygen site (*i.e.,* O43). A comparison between the unit-cell content of
501 kurnakovite (**c**) and kurnakovite-II (**d**) is also shown.

502

503

Table 1: Refined atomic fractional coordinates and isotropic displacement parameters (Å^2) of kurnakovite at selected pressures.

	P(GPa)	*x*	*y*	*z*	*Uiso* (Å^2)
Mg1	0.0001	0.6534(6)	0.2323(1)	0.8021(4)	0.012(3)
	4.43(5)	0.6532(5)	0.2352(4)	0.8024(4)	0.010(3)
	8.08(5)	0.6525(5)	0.2371(1)	0.8014(4)	0.009(2)
B1	0.0001	0.770(2)	0.2281(4)	0.351(1)	0.011(7)
	4.43(5)	0.765(2)	0.2300(4)	0.348(1)	0.008(5)
	8.08(5)	0.762(2)	0.2313(4)	0.344(1)	0.008(5)
B2	0.0001	0.109(2)	0.3528(4)	0.501(1)	0.011(6)
	4.43(5)	0.114(2)	0.3540(4)	0.506(1)	0.010(5)
	8.08(5)	0.115(2)	0.3535(4)	0.510(1)	0.009(5)
B3	0.0001	0.985(2)	0.1066(4)	0.314(1)	0.012(7)
	4.43(5)	0.984(2)	0.0977(4)	0.311(1)	0.011(6)
	8.08(5)	0.977(2)	0.0928(4)	0.306(1)	0.009(5)
O1	0.0001	0.922(1)	0.3219(3)	0.920(1)	0.029(8)
	4.43(5)	0.926(2)	0.3205(3)	0.926(1)	0.023(6)
	8.08(5)	0.925(1)	0.3228(3)	0.9294(9)	0.020(5)
O2	0.0001	0.593(1)	0.4095(3)	0.7767(9)	0.020(6)
	4.43(5)	0.586(1)	0.4158(3)	0.7702(9)	0.017(5)
	8.08(5)	0.579(1)	0.4181(3)	0.7636(8)	0.017(5)
O3	0.0001	0.385(3)	0.1355(3)	0.669(1)	0.022(6)
	4.43(5)	0.383(1)	0.1356(3)	0.6783(9)	0.017(6)
	8.08(5)	0.387(1)	0.1358(3)	0.6858(9)	0.016(5)
O4	0.0001	0.670(1)	0.0349(3)	0.808(1)	0.017(5)
	4.43(5)	0.665(1)	0.0274(3)	0.7984(9)	0.014(5)
	8.08(5)	0.667(1)	0.0254(3)	0.7932(8)	0.013(4)
O5	0.0001	0.650(1)	0.1916(3)	0.4734(9)	0.015(5)
	4.43(5)	0.646(1)	0.1921(3)	0.4717(8)	0.012(4)
	8.08(5)	0.642(1)	0.1923(3)	0.4698(8)	0.011(4)
O6	0.0001	0.671(1)	0.2635(3)	0.1436(8)	0.017(6)
	4.43(5)	0.667(1)	0.2738(3)	0.1421(8)	0.012(4)
	8.08(5)	0.662(1)	0.2788(3)	0.1407(8)	0.012(4)
O7	0.0001	0.812(1)	0.1030(3)	0.2692(9)	0.013(5)
	4.43(5)	0.804(1)	0.0990(3)	0.2547(9)	0.012(4)
	8.08(5)	0.804(1)	0.0990(3)	0.2489(8)	0.010(4)
O8	0.0001	0.932(1)	0.3339(3)	0.5043(8)	0.012(5)
	4.43(5)	0.935(1)	0.3376(3)	0.5088(8)	0.011(4)
	8.08(5)	0.930(1)	0.3391(3)	0.5035(8)	0.011(4)

O9	0.0001	0.152(1)	0.4407(3)	0.3558(8)	0.014(5)
	4.43(5)	0.156(1)	0.4428(3)	0.3566(8)	0.011(4)
	8.08(5)	0.165(1)	0.4444(3)	0.3616(7)	0.010(4)
O10	0.0001	0.252(1)	0.4094(3)	0.736(1)	0.025(7)
	4.43(5)	0.249(1)	0.4135(4)	0.7440(7)	0.021(5)
	8.08(5)	0.248(1)	0.4130(3)	0.7558(9)	0.016(5)
O11	0.0001	0.129(1)	0.2209(3)	0.4126(9)	0.016(5)
	4.43(5)	0.131(1)	0.2150(3)	0.416(1)	0.013(5)
	8.08(5)	0.131(1)	0.2115(3)	0.4169(8)	0.012(4)
O12	0.0001	0.018(1)	0.9876(3)	0.2495(9)	0.020(6)
	4.43(5)	0.014(1)	0.9721(3)	0.2480(7)	0.018(5)
	8.08(5)	0.019(1)	0.9624(3)	0.2477(9)	0.016(5)
O13	0.0001	0.291(1)	0.2447(3)	0.056(1)	0.027(7)
	4.43(5)	0.293(1)	0.2492(3)	0.0631(9)	0.018(5)
	8.08(5)	0.295(1)	0.2497(3)	0.0701(9)	0.015(4)

535 **Table 2:** Refined atomic fractional coordinates and isotropic displacement parameters (Å^2) of
536 kurnakovite-II at 11.11(5) GPa.
537

	x	*y*	*z*	*Uiso* (Å^2)
Mg11	0.742(5)	0.0257(4)	0.8858(5)	0.013(4)
Mg12	0.907(5)	0.6519(4)	0.4281(6)	0.014(4)
Mg13	0.452(5)	0.6909(4)	0.2551(5)	0.014(4)
B11	0.633(2)	0.913(1)	0.116(2)	0.01(1)
B12	0.010(2)	0.744(1)	0.197(2)	0.011(9)
B13	0.694(2)	0.441(1)	0.552(2)	0.01(1)
B21	0.861(2)	0.009(1)	0.253(2)	0.01(1)
B22	0.806(2)	0.665(1)	0.042(2)	0.01(1)
B23	0.483(2)	0.322(1)	0.403(2)	0.01(1)
B31	0.737(2)	0.156(1)	0.234(2)	0.01(1)
B32	0.907(2)	0.507(1)	0.082(2)	0.01(1)
B33	0.606(2)	0.188(1)	0.506(2)	0.01(1)
O11	0.895(1)	0.0849(9)	0.007(1)	0.023(8)
O12	0.748(1)	0.5464(8)	0.297(1)	0.019(7)
O13	0.632(1)	0.7420(8)	0.329(1)	0.021(8)
O21	0.776(1)	0.8876(8)	0.765(1)	0.019(8)
O22	0.886(1)	0.8063(8)	0.538(1)	0.019(8)
O23	0.448(1)	0.5432(8)	0.113(1)	0.017(7)
O31	0.415(1)	0.0074(8)	0.244(1)	0.015(7)
O32	0.086(1)	0.7224(9)	0.512(1)	0.022(9)
O33	0.256(1)	0.6457(8)	0.191(1)	0.018(8)
O41	0.684(1)	0.1695(8)	0.974(1)	0.019(8)
O42	0.954(1)	0.4862(8)	0.361(1)	0.018(8)
O43	0.446(1)	0.8500(8)	0.383(1)	0.016(8)
O51	0.148(1)	0.8235(8)	0.194(1)	0.015(7)
O52	0.821(1)	0.5527(8)	0.556(1)	0.014(7)
O53	0.512(1)	0.8143(7)	0.141(1)	0.014(7)
O61	0.631(1)	0.8887(8)	0.981(1)	0.018(8)
O62	0.975(1)	0.7818(8)	0.315(1)	0.015(7)
O63	0.367(1)	0.5396(7)	0.340(1)	0.013(7)
O71	0.634(1)	0.0530(8)	0.160(1)	0.014(7)
O72	0.985(1)	0.5967(8)	0.173(1)	0.013(7)
O73	0.288(1)	0.6844(7)	0.459(1)	0.014(7)
O81	0.743(1)	0.9026(8)	0.178(1)	0.019(9)
O82	0.932(1)	0.7675(8)	0.101(1)	0.014(7)
O83	0.606(1)	0.4361(8)	0.447(1)	0.013(7)
O91	0.977(1)	0.0213(8)	0.192(1)	0.015(7)
O92	0.702(1)	0.6473(7)	0.117(1)	0.013(8)
O93	0.628(1)	0.6784(8)	0.535(1)	0.015(7)
O101	0.889(1)	0.9778(8)	0.370(1)	0.020(9)
O102	0.767(1)	0.6999(8)	0.929(1)	0.018(8)
O103	0.439(1)	0.3196(9)	0.279(1)	0.021(9)
O111	0.849(1)	0.1404(8)	0.267(1)	0.016(8)
O112	0.817(1)	0.5308(8)	0.007(1)	0.017(8)
O113	0.500(1)	0.8037(8)	0.580(1)	0.016(8)
O121	0.728(1)	0.2790(8)	0.259(1)	0.029(8)
O122	0.904(1)	0.3778(8)	0.056(1)	0.029(8)
O123	0.642(1)	0.0844(7)	0.436(1)	0.016(8)
O131	0.580(1)	0.3476(8)	0.099(1)	0.029(9)

O132	0.207(1)	0.9829(9)	0.428(1)	0.022(8)
O133	0.073(1)	0.3360(8)	0.215(1)	0.019(8)

538
539
540

Table 3: Refined atomic fractional coordinates and equivalent displacement parameters (Å^2) of kurnakovite at selected temperatures.

	T(K)	*x*	*y*	*z*	*Ueq*
Mg1	100	0.65344(5)	0.23143(4)	0.80301(6)	0.0059(2)
	297	0.65288(7)	0.23211(6)	0.8013(1)	0.0140(3)
	373	0.65279(9)	0.23232(8)	0.8009(1)	0.0222(3)
B1	100	0.7685(2)	0.2262(1)	0.3512(2)	0.0060(4)
	297	0.7697(2)	0.2271(2)	0.3505(3)	0.0130(6)
	373	0.7706(3)	0.2276(2)	0.3513(4)	0.0207(8)
B2	100	0.1127(2)	0.3529(1)	0.5026(2)	0.0062(4)
	297	0.1108(2)	0.3527(2)	0.5011(3)	0.0139(6)
	373	0.1116(3)	0.3534(2)	0.5013(4)	0.0204(8)
B3	100	0.9823(2)	0.1048(1)	0.3098(2)	0.0063(4)
	297	0.9820(2)	0.1054(2)	0.3112(3)	0.0142(6)
	373	0.9824(3)	0.1062(2)	0.3123(4)	0.0217(8)
O1	100	0.9236(1)	0.3210(1)	0.9222(2)	0.0109(3)
	297	0.9208(2)	0.3214(1)	0.9190(3)	0.0263(6)
	373	0.9199(3)	0.3214(2)	0.9183(3)	0.0384(8)
O2	100	0.5971(1)	0.40949(9)	0.7826(2)	0.0096(3)
	297	0.5943(2)	0.4091(1)	0.7769(3)	0.0242(6)
	373	0.5938(3)	0.4091(2)	0.7740(4)	0.0347(8)
O3	100	0.3829(1)	0.13431(9)	0.6667(2)	0.0085(3)
	297	0.3833(2)	0.1348(1)	0.6686(2)	0.0207(5)
	373	0.3849(2)	0.1353(2)	0.6696(3)	0.0301(7)
O4	100	0.6691(1)	0.03425(8)	0.8070(2)	0.0079(3)
	297	0.6688(2)	0.0349(1)	0.8073(2)	0.0179(5)
	373	0.6701(2)	0.0357(2)	0.8076(3)	0.0271(7)
O5	100	0.6501(1)	0.19150(9)	0.4753(1)	0.0068(3)
	297	0.6513(2)	0.1924(1)	0.4737(2)	0.0162(5)
	373	0.6521(2)	0.1931(2)	0.4737(3)	0.0244(6)
O6	100	0.6687(1)	0.26157(9)	0.1415(1)	0.0076(3)
	297	0.6713(2)	0.2634(1)	0.1416(2)	0.0191(5)
	373	0.6727(3)	0.2645(2)	0.1427(3)	0.0280(7)
O7	100	0.8094(1)	0.10167(8)	0.2680(1)	0.0064(3)
	297	0.8102(2)	0.1031(1)	0.2675(2)	0.0149(5)
	373	0.8101(2)	0.1032(2)	0.2676(3)	0.0235(6)
O8	100	0.9338(1)	0.33384(8)	0.5063(1)	0.0065(3)
	297	0.9328(2)	0.3340(1)	0.5056(2)	0.0154(5)
	373	0.9321(2)	0.3332(2)	0.5049(3)	0.0236(6)

O9	100	0.1531(1)	0.44317(9)	0.3590(1)	0.0076(3)
	297	0.1492(2)	0.4400(1)	0.3542(2)	0.0179(5)
	373	0.1484(2)	0.4390(2)	0.3530(3)	0.0274(7)
O10	100	0.2527(1)	0.40606(9)	0.7394(2)	0.0088(3)
	297	0.2505(2)	0.4096(2)	0.7349(2)	0.0247(5)
	373	0.2484(3)	0.4096(2)	0.7330(3)	0.0358(8)
O11	100	0.1298(1)	0.22198(8)	0.4099(1)	0.0068(3)
	297	0.1285(2)	0.2214(1)	0.4137(2)	0.0166(5)
	373	0.1289(2)	0.2214(2)	0.4154(3)	0.0256(6)
O12	100	0.0156(1)	0.98708(9)	0.2466(2)	0.0088(3)
	297	0.0156(2)	0.9881(1)	0.2489(2)	0.0215(5)
	373	0.0162(2)	0.9892(2)	0.2498(3)	0.0312(7)
O13	100	0.2877(1)	0.2421(1)	0.0505(2)	0.0115(3)
	297	0.2861(2)	0.2431(2)	0.0519(3)	0.0302(7)
	373	0.2866(3)	0.2434(3)	0.0536(5)	0.044(1)
H1	100	0.998(4)	0.364(3)	0.063(5)	0.038
	297	0.987(5)	0.360(4)	0.056(7)	0.038
	373	0.998(5)	0.366(4)	0.051(8)	0.038
H2	100	0.967(4)	0.333(3)	0.817(5)	0.038
	297	0.979(4)	0.335(4)	0.817(6)	0.038
	373	0.960(5)	0.332(4)	0.828(7)	0.038
H3	100	0.656(4)	0.466(3)	0.719(5)	0.038
	297	0.678(5)	0.470(4)	0.714(6)	0.038
	373	0.680(5)	0.477(4)	0.734(7)	0.038
H4	100	0.487(4)	0.414(3)	0.755(4)	0.038
	297	0.477(5)	0.417(4)	0.756(6)	0.038
	373	0.487(6)	0.406(4)	0.742(7)	0.038
H5	100	0.310(4)	0.165(3)	0.588(5)	0.038
	297	0.311(5)	0.167(4)	0.585(6)	0.038
	373	0.313(5)	0.161(4)	0.593(7)	0.038
H6	100	0.328(4)	0.062(3)	0.683(5)	0.038
	297	0.321(4)	0.059(4)	0.692(6)	0.038
	373	0.322(5)	0.059(4)	0.692(7)	0.038
H7	100	0.754(4)	0.024(3)	0.770(5)	0.038
	297	0.756(5)	0.022(4)	0.768(6)	0.038
	373	0.758(5)	0.031(4)	0.767(7)	0.038
H8	100	0.698(4)	0.037(3)	0.946(5)	0.038
	297	0.696(5)	0.040(4)	0.936(7)	0.038

	373	0.693(5)	0.041(4)	0.938(8)	0.038
H9	100	0.549(4)	0.127(3)	0.389(5)	0.038
	297	0.547(5)	0.132(4)	0.398(6)	0.038
	373	0.570(6)	0.139(4)	0.387(7)	0.038
H10	100	0.566(4)	0.259(3)	0.139(4)	0.038
	297	0.576(5)	0.262(4)	0.146(6)	0.038
	373	0.581(6)	0.260(4)	0.145(7)	0.038
H11	100	0.121(3)	0.511(3)	0.397(5)	0.038
	297	0.131(5)	0.501(4)	0.382(6)	0.038
	373	0.125(5)	0.500(4)	0.395(7)	0.038
H12	100	0.265(3)	0.486(3)	0.797(5)	0.038
	297	0.240(4)	0.495(4)	0.801(6)	0.038
	373	0.257(6)	0.468(5)	0.778(8)	0.038
H13	100	0.926(4)	0.921(3)	0.168(5)	0.038
	297	0.927(5)	0.920(4)	0.178(6)	0.038
	373	0.932(5)	0.929(5)	0.174(7)	0.038
H14	100	0.259(4)	0.262(3)	0.158(5)	0.038
	297	0.272(4)	0.258(4)	0.165(7)	0.038
	373	0.272(5)	0.267(4)	0.174(7)	0.038
H15	100	0.273(3)	0.298(3)	0.967(5)	0.038
	297	0.257(4)	0.292(4)	0.964(6)	0.038
	373	0.274(5)	0.295(5)	0.980(7)	0.038

564 **Table 4**: Selected statistical parameters pertaining to the structure refinements of kurnakovite based
565 on the intensity XRD data collected at varying temperatures and pressures.
566

T (K)	Unique reflections	Observed reflections $I > 3\sigma(I)$	Refined variables	R_{int} (Friedel-all)	R_1 (obs)	R_1 (all)	wR_1 (obs)
100	2351	2273	197	2.9	0.0444	0.0451	0.0642
120	2374	2294	197	6.6	0.0533	0.0540	0.0832
140	2377	2307	197	6.7	0.0552	0.0559	0.0933
160	2372	2297	197	6.2	0.0499	0.0505	0.0731
180	2374	2300	197	6.5	0.0483	0.0489	0.0713
200	2384	2308	197	6.2	0.0531	0.0542	0.0898
220	2385	2308	197	6.0	0.0540	0.0548	0.0871
240	2385	2300	197	6.5	0.0537	0.0547	0.0836
260	2389	2298	197	6.3	0.0530	0.0540	0.0808
280	2395	2291	197	6.6	0.0539	0.0555	0.0830
297	2297	2287	197	6.4	0.0565	0.0566	0.0875
353	2321	2315	197	7.4	0.0529	0.0542	0.1004
373	2315	2302	197	7.5	0.0588	0.0606	0.1161
P (GPa)							
0.0001	1573	945	69	3.4	0.0790	0.1289	0.0850
1.07(5)	1523	1173	69	2.0	0.0899	0.1099	0.1022
1.83(5)	1511	1202	69	2.2	0.0833	0.0989	0.1020
3.21(5)	1474	956	69	3.1	0.0895	0.1332	0.0928
4.43(5)	1448	1116	69	5.6	0.0861	0.1022	0.1178
5.35(5)	1411	1001	69	2.1	0.0829	0.1066	0.0909
6.54(5)	1391	919	69	3.3	0.0850	0.1112	0.0916
8.08(5)	1381	1076	69	2.6	0.0795	0.0950	0.0967
9.23(5)	1353	975	69	3.3	0.0810	0.1034	0.0956
11.11(5)	2791	1752	205	5.5	0.0764	0.1169	0.0802
12.21(5)	2442	1159	205	7.4	0.0962	0.1798	0.0986

567
568

569 **Table 5:** Unit-cell parameters of kurnakovite with temperature.
570

T (K)	V (Å^3)	a (Å)	b (Å)	c (Å)	α (°)	β (°)	γ (°)
100	495.49(5)	8.3152(2)	10.5959(8)	6.4187(5)	99.000(6)	109.026(5)	105.773(5)
120	495.81(5)	8.3167(2)	10.5969(7)	6.4199(4)	98.991(5)	109.020(5)	105.763(5)
140	496.10(5)	8.3186(2)	10.6001(7)	6.4208(4)	98.981(5)	109.011(5)	105.765(5)
160	496.59(5)	8.3208(2)	10.6003(7)	6.4228(4)	98.967(5)	109.007(5)	105.752(5)
180	497.09(5)	8.3233(2)	10.6000(7)	6.4254(4)	98.960(5)	109.001(5)	105.727(5)
200	497.55(5)	8.3261(2)	10.5994(7)	6.4280(4)	98.942(5)	108.994(5)	105.705(5)
220	498.09(5)	8.3294(2)	10.5990(7)	6.4308(4)	98.929(5)	108.987(4)	105.679(5)
240	498.65(5)	8.3327(2)	10.5987(7)	6.4338(4)	98.913(5)	108.985(4)	105.652(4)
260	499.23(5)	8.3363(2)	10.5988(7)	6.4365(4)	98.900(5)	108.981(4)	105.625(4)
280	499.86(5)	8.3401(2)	10.5992(7)	6.4397(4)	98.897(5)	108.985(4)	105.599(4)
297	500.52(5)	8.3442(2)	10.6002(7)	6.4427(4)	98.865(5)	108.980(4)	105.577(4)
353	502.37(4)	8.3559(2)	10.6062(6)	6.4490(4)	98.805(5)	108.972(4)	105.525(4)
373	503.21(4)	8.3612(2)	10.6109(6)	6.4514(4)	98.787(5)	108.972(4)	105.507(4)
393	506.7(6)	8.38(5)	10.631(7)	6.480(5)	98.67(6)	109.14(7)	105.62(6)

571
572

573 **Table 6:** Unit-cell parameters of kurnakovite and kurnakovite-II with pressure (*: data collected in
574 decompression).
575

P (GPa)	*V* (Å^3)	*a* (Å)	*b* (Å)	*c* (Å)	α (°)	β (°)	γ (°)
0.0001	497.9(5)	8.308(7)	10.599(2)	6.442(3)	98.85(3)	109.09(6)	105.57(4)
1.07(5)	485.1(2)	8.274(3)	10.4270(7)	6.3957(7)	99.031(9)	109.01(2)	105.29(2)
1.83(5)	477.2(2)	8.227(3)	10.341(1)	6.3697(9)	99.11(1)	109.00(2)	105.16(2)
3.21(5)	463.3(2)	8.168(3)	10.192(1)	6.320(1)	99.22(1)	109.01(2)	104.86(2)
4.43(5)	453.4(2)	8.125(3)	10.0830(7)	6.2764(9)	99.309(9)	108.95(2)	104.67(1)
5.35(5)	446.6(2)	8.088(3)	10.0110(6)	6.247(1)	99.356(9)	108.93(2)	104.47(1)
6.54(5)	437.9(2)	8.047(3)	9.9193(9)	6.2068(9)	99.41(1)	108.90(2)	104.29(2)
8.08(5)	431.5(2)	8.023(3)	9.8404(8)	6.1725(9)	99.46(1)	108.78(2)	104.10(1)
9.23(5)	424.0(2)	7.978(3)	9.7603(8)	6.141(1)	99.49(1)	108.80(2)	103.87(2)
11.11(5)	1212.8(3)	11.011(2)	10.827(2)	11.286(2)	99.65(1)	93.96(2)	112.45(2)
12.21(5)	1199.5(8)	10.967(4)	10.788(4)	11.237(4)	99.64(3)	93.90(3)	112.34(4)
13.63(5)	1150(4)	10.88(2)	10.64(2)	11.031(2)	99.46(2)	95.31(2)	112.0(2)
10.80(5)*	1186(5)	11.00(2)	10.74(2)	11.14(3)	100.0(2)	94.8(2)	112.1(2)
8.29(5)*	1211(7)	11.04(4)	10.85(4)	11.24(3)	99.9(3)	94.9(3)	112.3(3)

576
577

Table 7: Mg1-O bond distances (in Å), based on the structure refinements of kurnakovite at high pressure. Volumes of Mg1- and B-coordination polyhedra (in Å^3; calculated using the routine implemented in the software *Vesta* [50]), based on the structure refinements at high pressure.

P (GPa)	0.0001	1.07(5)	1.83(5)	3.21(5)	4.43(5)	5.35(5)	6.54(5)	8.08(5)	9.23(5)
Mg1-O1	1.996(11)	1.987(11)	1.986(11)	2.018(13)	1.985(12)	1.993(12)	1.952(13)	1.971(11)	1.969(12)
Mg1-O2	2.085(6)	2.068(6)	2.069(6)	2.053(7)	2.053(6)	2.036(7)	2.044(7)	2.032(6)	2.029(7)
Mg1-O3	2.002(11)	2.026(11)	2.020(10)	1.980(10)	1.986(10)	1.957(11)	1.960(10)	1.949(11)	1.933(11)
Mg1-O4	2.139(5)	2.121(5)	2.118(5)	2.121(6)	2.118(5)	2.108(5)	2.104(5)	2.108(5)	2.101(5)
Mg1-O5	2.084(7)	2.067(6)	2.057(6)	2.046(8)	2.027(7)	2.024(7)	2.003(7)	1.991(6)	1.982(7)
Mg1-O6	2.123(7)	2.104(6)	2.096(6)	2.089(8)	2.065(7)	2.068(7)	2.046(7)	2.039(6)	2.025(7)
V_{Mg1}	11.78(6)	11.63(6)	11.55(6)	11.44(6)	11.22(6)	11.09(6)	10.87(6)	10.81(5)	10.66(6)
V_{B1}	1.639(6)	1.653(6)	1.651(6)	1.627(7)	1.623(6)	1.601(5)	1.615(6)	1.584(5)	1.594(5)
V_{B2}	1.650(8)	1.629(8)	1.616(8)	1.601(9)	1.574(8)	1.597(8)	1.574(8)	1.584(7)	1.586(8)

Table 8: Two relevant angles (in °) based on the structure refinements of kurnakovite at high pressure.

P (GPa)	B1-Mg1-B1 (°)	O12-O12-O12 (°)
0.0001	147.7(6)	164.5(6)
1.07(5)	147.9(5)	162.9(6)
1.83(5)	148.0(5)	160.9(6)
3.21(5)	148.5(6)	157.7(3)
4.43(5)	148.8(6)	156.4(2)
5.35(5)	147.6(5)	154.5(5)
6.54(5)	148.8(6)	152.9(5)
8.08(5)	149.2(6)	151.2(4)
9.23(5)	149.2(5)	150.1(5)

Fig. 1

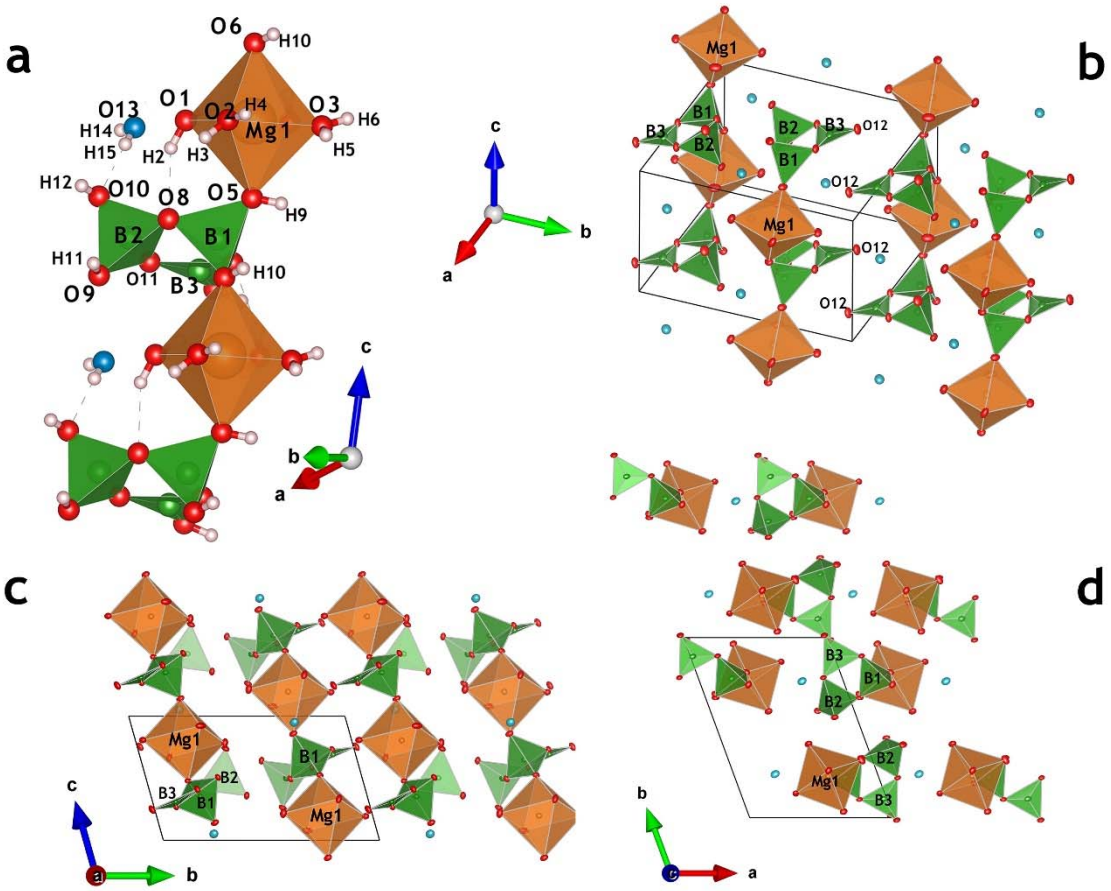
a
O6
H10
O13
O1
O2
H4
O3
H6
H14
Mg1
H15
H2
H3
H5
H12
O10
O8
O5
H9
B2
B1
H11
O11
B3
H10
O9
c
b
a
b
Mg1
B1
B3
B2
O12
B2
B3
O12
B1
O12
Mg1
O12
O12
c
d
c
Mg1
B1
B3
B2
B1
Mg1
b
a
B3
B1
B2
B2
Mg1
B3
b
a

Fig. 2

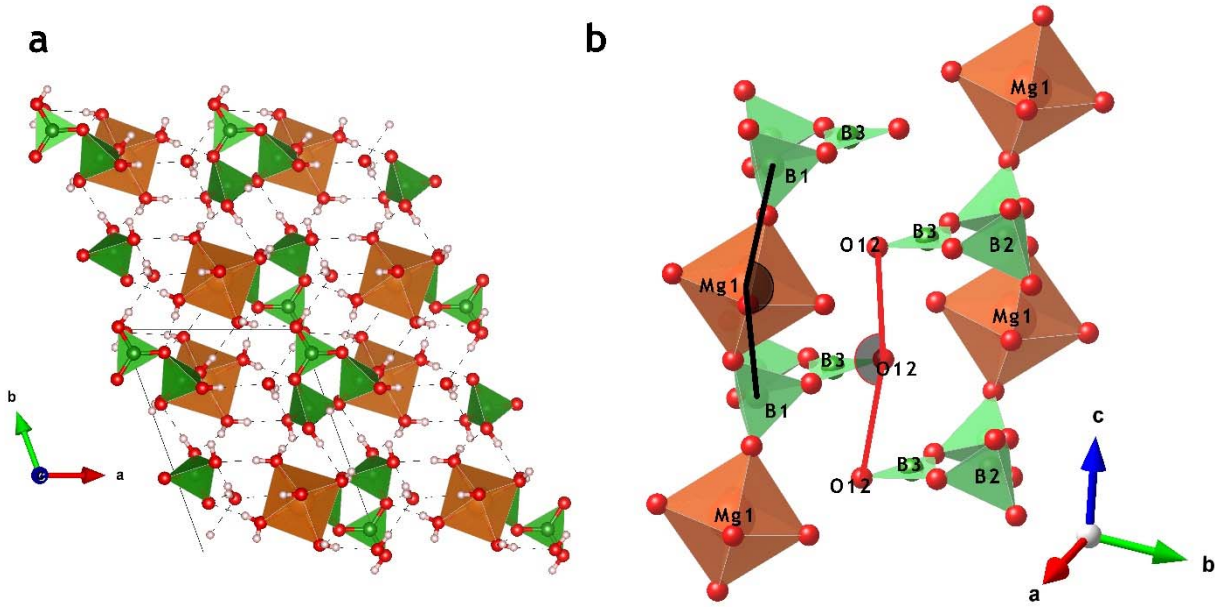

Fig. 3

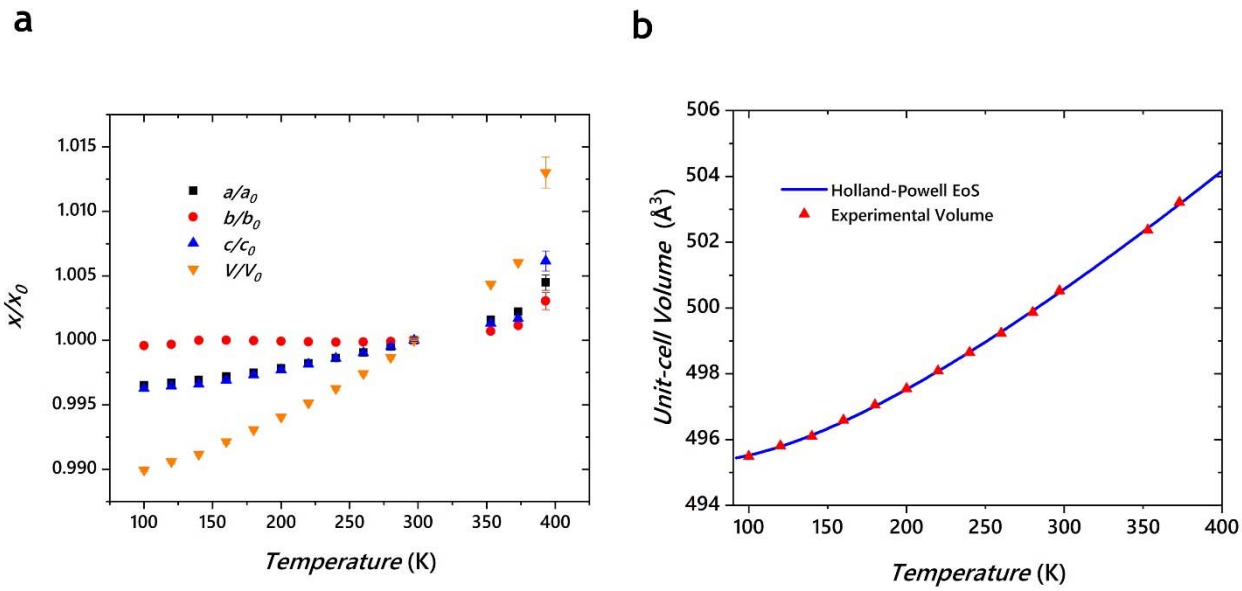
a
b
1.015
1.010
1.005
1.000
0.995
0.990
x/x0
a/a0
b/b0
c/c0
V/V0
100
150
200
250
300
350
400
Temperature (K)
506
504
502
500
498
496
494
Unit-cell Volume (Å3)
Holland-Powell EoS
Experimental Volume
100
150
200
250
300
350
400
Temperature (K)

Fig. 4

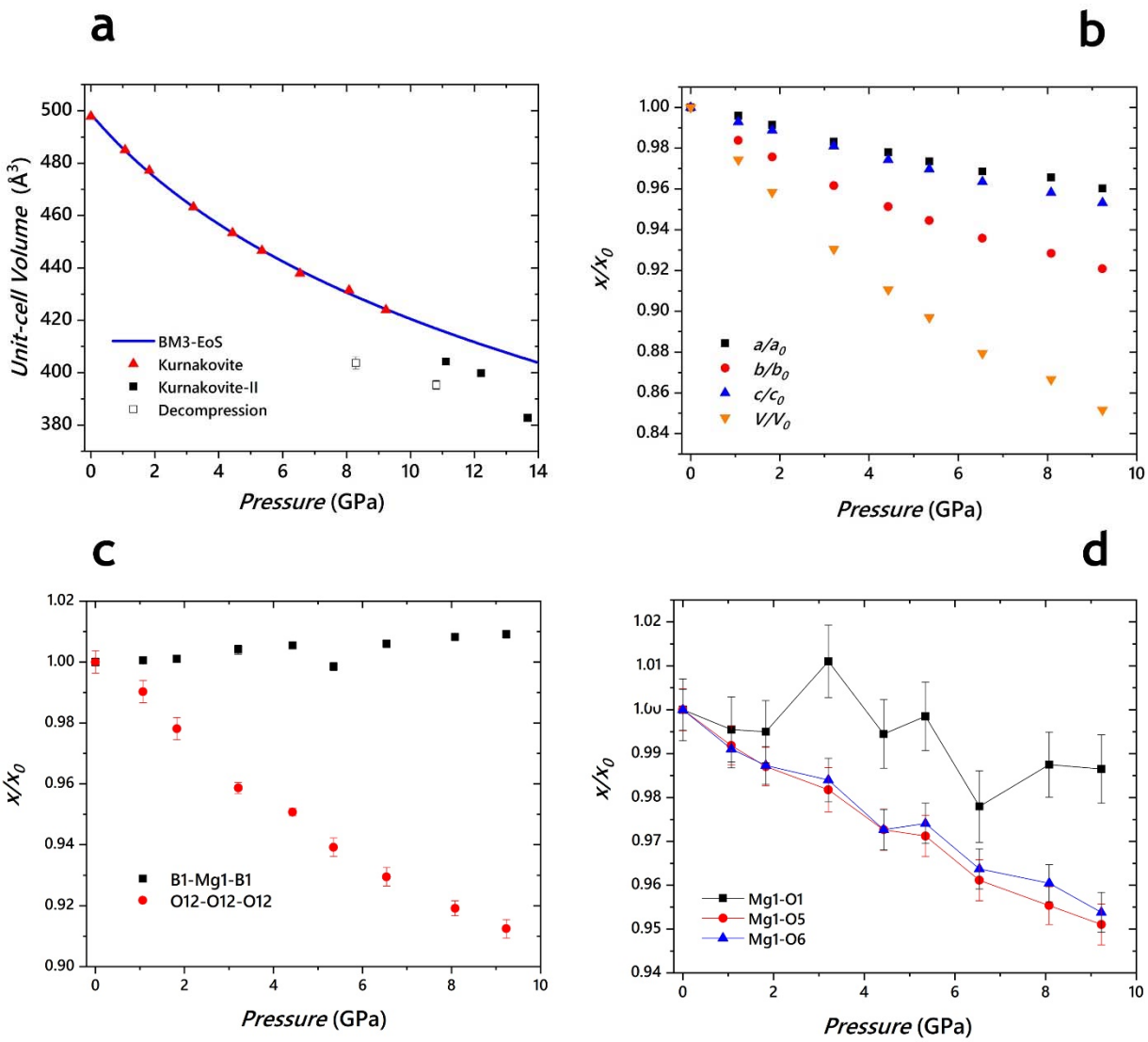
a
b
500
480
460
440
420
400
380
Unit-cell Volume (Å3)
BM3-EoS
Kurnakovite
Kurnakovite-II
Decompression
0
2
4
6
8
10
12
14
Pressure (GPa)
1.00
0.98
0.96
0.94
0.92
0.90
0.88
0.86
0.84
x/x0
a/a0
b/b0
c/c0
V/V0
0
2
4
6
8
10
Pressure (GPa)
c
d
1.02
1.00
0.98
0.96
0.94
0.92
0.90
x/x0
B1-Mg1-B1
O12-O12-O12
0
2
4
6
8
10
Pressure (GPa)
1.02
1.01
1.00
0.99
0.98
0.97
0.96
0.95
0.94
x/x0
Mg1-O1
Mg1-O5
Mg1-O6
0
2
4
6
8
10
Pressure (GPa)

Fig. 5

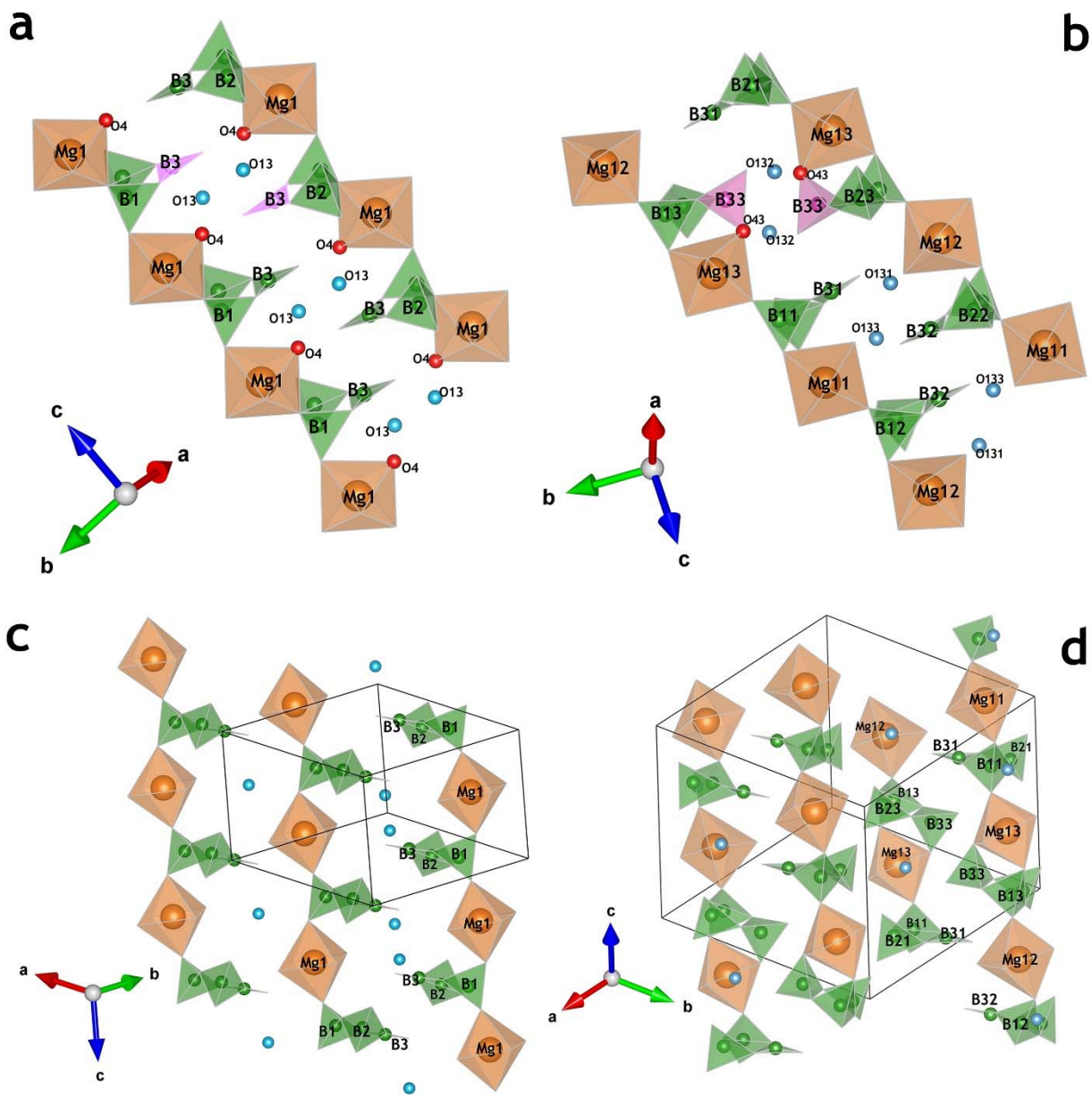
a
B3
B2
Mg1
O4
O13
B1
c
a
b
b
B21
B31
Mg13
Mg12
O132
O43
B13
B33
B23
O131
B11
B22
O133
Mg11
B12
c
d

778
779
780
781
782
783
784
785
786